J. Fluid Mech. (2006), *vol.* 567, *pp.* 433–455. © 2006 Cambridge University Press
doi:10.1017/S0022112006002011 Printed in the United Kingdom

An experimental study of surfactant effects on spilling breakers

By XINAN LIU AND JAMES H. DUNCAN

Department of Mechanical Engineering, University of Maryland, College Park, MD 20742, USA

(Received 15 October 2004 and in revised form 15 March 2006)

The dynamics of spilling breakers in the presence of surfactants were studied experimentally. The spilling breakers were produced from Froude-scaled mechanically generated dispersively focused wave packets with average frequencies of 1.15, 1.26 and 1.42 Hz. Separate experiments were performed with the same wave-maker motions in clean water and in water with various bulk concentrations of the soluble surfactants sodium dodecyl sulfate (SDS) and Triton X-100 (TX). For nearly all surfactant conditions, the surface-pressure isotherm, equilibrium surface elasticity and surface viscosity were measured *in situ* in order to characterize the dynamic properties of the free surface. In clean water, all the waves considered herein break without overturning of the free surface. This breaking process begins with the formation of a bulge on the forward face of the wave crest and capillary waves upstream of the leading edge of the bulge (called the toe). After a short time, the flow separates under the toe and a turbulent flow is developed while the toe moves rapidly down the wave face. During the toe motion, a train of ripples appears between the toe and the crest and this train of ripples is swept downstream. In the presence of surfactants, the bulge shape is modified and its size generally decreases with increasing surfactant concentration. The capillary waves found upstream of the toe in the clean-water case are dramatically reduced at even the lowest concentrations of surfactants. With surfactants, the start of the breaking process is still initiated when the toe begins to move down the forward face of the wave. The pattern of ripples generated between the toe and the crest of the wave during this phase of the breaking process varies with the concentration of surfactant. It was found that the temporal history of the vertical distance between the toe and the wave crest scales with the nominal length $(\sigma_0/\rho g)^{1/2}$ while the bulge length from toe to crest scales with the nominal length $(\mu_s/\rho\sqrt{g})^{2/5}$, where σ_0 and μ_s are the ambient surface tension and the surface viscosity, respectively.

1. Introduction

Numerical simulations have shown that, without surface tension, weak spilling breakers generated by wave–wave interactions (Tulin 1996) and the evolution of steep waves (Longuet-Higgins & Dommermuth 1997) are initiated by a small jet that issues from the crest and plunges into the front wave face at a height well above the mean water level. In clean (i.e. surfactant-free) water, surface tension causes dramatic changes in this behaviour when the breaking is very weak and/or the wavelength is short; see Ebuchi, Wawamura & Toba (1987), Longuet-Higgins (1992), Duncan *et al.* (1994*a*, *b*, 1999), Longuet-Higgins (1996), Yao, Wang & Tulin (1996), Tulin (1996), Longuet-Higgins & Dommermuth (1997), Longuet-Higgins (1997), Ceniceros & Hou (1999) and the review by Duncan (2001). In these surface-tension-dominated breaking

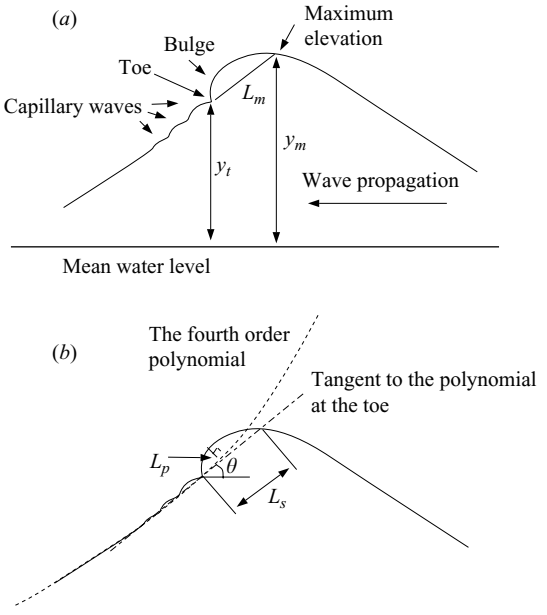

FIGURE 1. Schematic showing the nomenclature for the breaking-wave profile.

events, a bulge forms on the forward face of the crest and capillary waves appear upstream of the leading edge (called the toe) of the bulge; see figure 1. This ripple pattern quickly grows in amplitude. Particle-image velocimetry measurements (Qiao & Duncan 2001) indicate that the transition to turbulence occurs when the flow separates as it attempts to negotiate the highly curved free surface at the toe. It is likely that this process is controlled by the viscous free-surface boundary layer generated by the capillary waves, as calculated by Longuet-Higgins (1992). Subsequent to the initial separation, the fluid in the bulge appears to slide down the front face of the wave, creating a near-surface shear layer (Okuda 1982; Lin & Rockwell 1994; Lin & Rockwell 1995; Coakley 1997; Dabiri & Gharib 1997; Qiao & Duncan 2001) that contributes to the generation of ripples on the crest (Longuet-Higgins 1994). These ripples initially move at the speed of the crest but quickly slow down and are left behind the crest.

Pure water is never found in nature and is nearly impossible to obtain in the laboratory. Many of the ubiquitous contaminants in water are surface-active materials known as surfactants. Generally, the molecules of surfactants possess a bipolar structure composed of hydrophobic and hydrophilic segments (Edwards, Brenner & Wasan 1991). Surfactant molecules are adsorbed at an interface separating aqueous and non-aqueous phases. As a result, in the interfacial region a surfactant surface-excess layer, i.e. a monolayer, is formed. The surfactant monolayer is a compressible surface film that lowers the surface tension and creates surface elasticity and also surface viscosity (both dilational and shear); see for example Edwards *et al.* (1991). All these properties depend on the instantaneous local concentration of surfactants. The surface stresses due to the surface elasticity and viscosity and the gradients in the surface tension are balanced by subsurface viscous stresses.

Given the above-noted importance of surface tension in weak and/or short-wavelength spilling breakers in clean water, it is not surprising that surfactants

can have a strong influence on these waves. Field and laboratory experiments (Cox & Munk 1954; Lombardini *et al.* 1989; Barger *et al.* 1970; Hühnerfuss *et al.* 1983; Ermakov *et al.* 1986; Tang & Wu 1992; Bock *et al.* 1999; Uz *et al.* 2002; Mitsuyasu & Honda 1984) have shown that surfactants reduce the high-frequency part of the wind-wave spectrum. The effects of the film elasticity and surface viscosity on wind-wave growth and damping rates were studied numerically by Creamer & Wright (1992), who showed that the damping rate is substantially increased by the film elasticity and that the effect of the surface viscosity is more pronounced at larger wavenumbers when the surface elasticity is small. Lucassen (1981) demonstrated that the surface-dilational modulus has a considerable effect on the damping of short gravity waves and gravity capillary waves. The effects of surfactants on the formation of the bulge and the capillary waves in the early stages of weak spilling breakers was investigated by Ceniceros (2003) through a numerical simulation of the Navier–Stokes equations and the surface advection–diffusion equation. A linear relationship (with slope β) between the local surfactant concentration and the local surface tension was used and calculations for various values of β and Péclet number were performed. (The Péclet number is inversely proportional to the surfactant diffusion coefficient.) It was found that surfactants accumulate in the crest region, particularly in high-Péclet-number (weak-diffusion) cases. When the Péclet number is low, the size of the bulge and the amplitude and wavelength of the capillary waves decrease as β increases. When the Péclet number is high, the bulge and the capillary waves are greatly diminished. In a recent experimental study, Liu & Duncan (2003) found that under some surfactant conditions waves that broke by the flow-separation mechanism described above instead formed a small plunging jet that issued from the front face of the wave at a point below the wave crest. The jet projects forward entrapping a pocket of air upon impact with the front face of the wave. These plunging-jet cases were found at the end of a series of experiments, when an additional surfactant condition was allowed to develop; see § 2.5 for details.

In this paper, the dynamics of spilling breakers occurring in the presence of ambient surfactants was studied experimentally. Spilling breakers were generated mechanically with a dispersive focusing technique. In the overall study, five different generation conditions were used to produce waves with three different frequencies and three wave amplitudes. In the interests of brevity, however, results are given here for only one of these wave-maker motions. The water in the wave tank was mixed with soluble surfactants (sodium dodecyl sulfate (SDS) or Triton X-100) and experiments were performed with several bulk concentrations of each surfactant for each wave-maker motion. The surface-mechanical properties of the surfactants were measured *in situ* by using a longitudinal-wave-propagation technique and a Wilhelmy plate. The crest-profile histories of the breakers were measured using a photographic technique that employs a laser light sheet, fluorescent dye and a high-speed movie camera. The geometric characteristics of the crest profiles were correlated with the surface-property measurements in order to gain insight into the role of surfactants in the breaking process.

The remainder of this paper is divided into five sections. In § 2, the experimental setup and measurement techniques are described. The results of the measurements of surface-dynamic properties are presented in § 3 and the results for breakers from a single wave-maker motion in clean water and in the Triton X-100 solutions are presented in § 4. These results are discussed and compared in § 5. Finally, the conclusions are given in § 6.

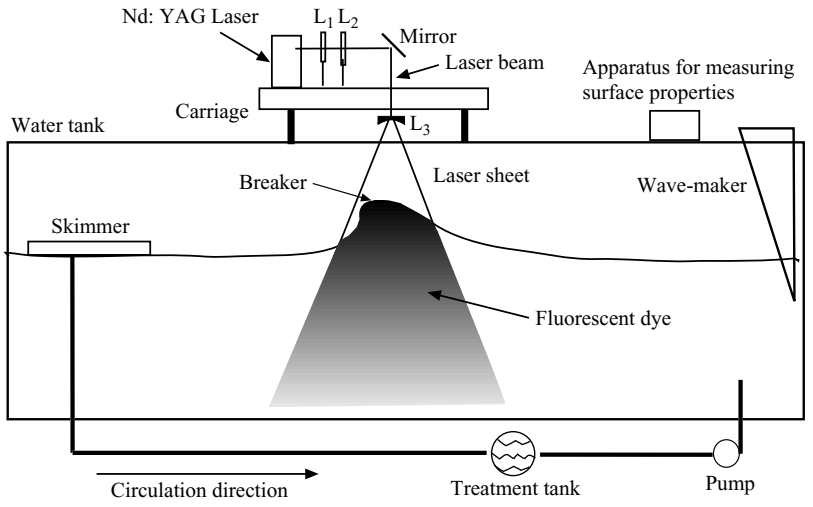

FIGURE 2. Schematic showing a side view of the tank, wave-maker, carriage and light sheet. Two convex cylindrical lenses (L_1 and L_2) are used to adjust the thickness of the light sheet at the mean water level, and a concave cylindrical lens L_3 is used to convert the laser beam into a laser sheet.

2. Experimental setup

2.1. *Wave generation*

The experiments were carried out in a wave tank 14.8 m long by 1.22 m wide with water depth 0.8 m (figure 2). The waves were generated mechanically by a vertically oscillating wedge located at one end of the tank, and a beach located at the opposite end of the tank was used to dissipate the wave energy. The wedge spanned the width of the tank and had a downward right-triangle cross-section. The side of the wedge facing the beach was inclined at an angle of 30° from the vertical. The wedge was driven by a ball screw and servo-motor mechanism and a computer-based feedback control system was used with a position sensor and a tachometer to control the motion of the wedge precisely.

The breaking-wave generation method (i.e. the dispersive focusing technique; see also Longuet-Higgins 1974 and Rapp & Melville 1990) and the wave-maker-motion parameters were identical to those described in Duncan *et al.* (1999). Five wave-maker motions were used in this study and for each case the values of the average frequency of the wave packet, f_0, and the non-dimensional amplitude of the wave-maker motion, A/λ_0 (where A is the overall amplitude and $\lambda_0 = g/(2\pi f_0^2)$ is the wavelength of the average frequency according to linear wave theory) can be found in table 1. This table also shows the measured (see § 2.2) non-dimensional clean-water crest height of the breakers, H_c/λ_0, where H_c is the vertical distance between the mean water level and the wave crest at the instant just before breaking begins (its maximum value). As can be seen from the table, H_c/λ_0 varies from 0.065 to 0.07 (a variation 7.3 % of its mean) while the non-dimensional amplitude of the wave-maker motion A/λ_0 varies from 0.0487 to 0.0505 (a variation of only 3.6 % of its mean). Also shown in the table is the wave-crest speed, which will be discussed in following subsection. In this paper, results are given only for the wave generated with $f_0 = 1.15$ Hz, the first line in the table. Readers interested in results for the other waves are referred to Liu (2002).

f_0 (Hz)	λ_0 (cm)	A/λ_0	H_c/λ_0	U (cm s^{-1})
1.15	118.06	0.0505	0.070	112.8
1.26	98.34	0.0505	0.070	102.1
1.42	77.43	0.0505	0.070	94.5
1.42	77.43	0.0496	0.066	94.5
1.42	77.43	0.0487	0.065	94.5

TABLE 1. The parameters of the five wave-maker motions used in this study. In this table, f_0 is the average frequency of the wave packet, $\lambda_0 = 2g/(2\pi f_0^2)$ is the wavelength of the average frequency according to linear wave theory, A/λ_0 is the non-dimensional overall amplitude of the wave-maker motion, H_c/λ_0 is the measured maximum non-dimensional crest height of the breaker and U, the crest speed, is the carriage speed at which the high-speed movies were taken.

2.2. *Wave measurement*

2.2.1. *The wave profile measurement*

The profiles of the breaking waves were measured photographically with a high-speed digital camera (Phantom IV, Photographic Analysis Co.). The camera records 512-by-512-pixel images with 8 bit grey levels at 300 images per second (frame rates up to 1000 images per second are possible). The camera was mounted on an instrument carriage that rides above the tank and is driven by a towing wire and a separate servo-motor. The camera was oriented to view the wave from the side with a look-down angle of about 5° from the horizontal (figure 5 in Duncan *et al.* 1999). This viewing angle gives the best measurements of the crest shape before and during the transition to turbulence. A 60 mm Nikon AF lens was used and at the centre line of the wave tank the field of view of the camera was about 16 cm horizontally.

The wave crest was illuminated with a light sheet from an Nd:YAG laser (Clark MXR ORC-1000). The laser was set to produce 10 000 2.5-mJ pulses per second. The laser head was mounted on the top of the instrument carriage and the laser beam was converted into a laser sheet by a concave cylindrical lens L_3 (see figure 2). Two convex cylindrical lenses (L_1 and L_2) were used to adjust the thickness of the light sheet and a mirror was used to direct the light sheet to the water surface. As a result of this optical system, the light sheet was oriented vertically along the centre plane of the tank and was 25 cm wide and 1 mm thick at the mean water level.

The light source for the photographs was the glowing fluorescent dye (either Rhodamine B with 70 % purity at a concentration of 2–3 p.p.m. or Rhodamine 6G with 95 % purity at a concentration of 0.1 p.p.m.) within the light sheet. A long-pass optical filter was placed in front of the camera lens to reject the specular reflections of laser light from the water surface while accepting the light from the fluorescing dye. With this illumination, the intersection of the light sheet and the water surface along the centreline of the tank was easily discernible in each image from the high-speed camera.

Crest-profile measurements were taken from the moving instrument carriage in a crest-fixed reference frame. The motion of the carriage was controlled by the same computer that controlled the wave maker. The carriage speed (accuracy ± 0.1 %) was controlled by a feedback loop using an optical encoder on the motor shaft. To create synchronized wave-maker and carriage motions for each wave studied, movies of the wave crests were taken with the system described above, while varying the carriage starting position, the starting time relative to the wave-maker motion, the acceleration

and the final speed from run to run. It should be kept in mind that the wave crest is deforming during breaking and that therefore the speed of the crest is not precisely defined. The final carriage speeds are given in table 1.

In order to determine the position of the breaking-wave crest in the tank in any frame of the high-speed movies, a microswitch attached to the top of the tank wall was used to trigger a flash lamp. The microswitch was activated by the passing of the carriage. This created a light mark in one image of the movie recorded by the high-speed camera. At the instant when any image of the wave was recorded, the position of the wave relative to the tank was computed by multiplying the carriage speed by the time interval between the image of the wave and the image with the light mark.

2.2.2. *Wave-profile extraction*

To extract the profile of the wave crest from each image (the upper edge of the wavy light region, see figure 6) in the high-speed movies, a program written in the programming language IDL was used. In the program, the extraction procedure consisted of several steps. First, in order to obtain a uniform dark background and enhance the image intensity, a threshold function was used to convert all grey levels below some value into black, i.e. zero image-intensity. Next, a smoothing function and gradient operator were used to obtain a gradient intensity at each pixel. The pixels with the highest values of image-intensity gradient on the upper edge of the light region were connected successively from left to right in the image and this line was taken as the surface profile.

The accuracy of the wave-profile extraction depends on the quality of the image and the phase of the breaking process in the image. In the well-focused images typical of this study, the free surface can be located to within one pixel (0.3 mm in the physical plane) before transition to turbulent flow and to within two or three pixels (0.6–1.0 mm in the physical plane) in the presence of turbulence that is strong enough to eject water droplets into the air. These accuracies also apply to the geometrical length parameters described later in this paper including the random component due to run-to-run variability.

2.3. *The water treatment*

At the beginning of each experiment, the tank was filled with filtered tap water and hypochlorite was added at a concentration of 10 p.p.m. to neutralize organic materials. A water skimming and circulation system was then used for a period of at least two days to purify the water further (figure 2). In this system, the tank water is removed through two surface skimmers at the end of the tank farthest from the wave maker. From the skimmers, the water goes to a separate treatment tank where air or ozone is bubbled through it to bring soluble surfactants to the surface. To remove these surfactants the water surface is skimmed and fresh water is added to the treatment tank through a 0.5 micron filter to make up for the skimmed water. The cleaned water is then pumped through a diatomaceous earth filter and back into the wave tank at the end near the wave maker. Just before the wave-breaking experiments began, the free chlorine level in the tank was reduced to zero by the addition of an appropriate amount of hydrogen peroxide and a fluorescent dye was mixed with the water for visualization purposes. The reduction in chlorine level was necessary to preserve the dye.

When a relatively clean free surface was desired, the water skimming and filtration system was turned on periodically during the experiments to maintain a low level of naturally occurring surfactants in the wave tank. When artificial surfactants were

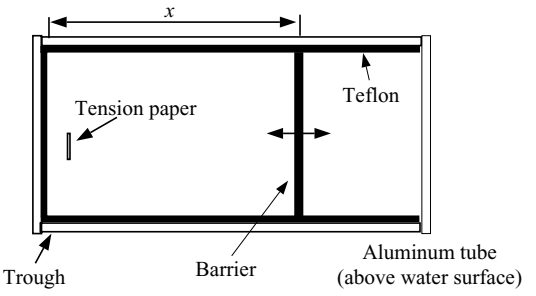

FIGURE 3. Schematic showing the plan view of the Langmuir trough setup to measure the surface-pressure isotherm.

added to the wave tank, all water-purification techniques were stopped except during the mixing process.

It is important to realize that, even with the above water-treatment procedures, these experiments were not performed with solutions of pure water and a single type of surfactant (sodium dodecyl sulfate or Triton X-100). The water in the tank is not distilled the dye and the surfactants added to the tank water probably contain other surfactants and additional surfactants probably enter the tank by various paths. Also, once the chlorine level is reduced to near zero, bacteria in the tank begin to grow. Bacteria are a type of plankton and are known to produce surface-active organic material as byproducts of their respiration; see Frew (1997). In view of these difficulties, the results of this study are viewed as a correlation of the wave behaviour with the measured dynamic properties of the surface rather than with the chemical composition of the surfactants.

2.4. *Surface-property measurements*

In order to characterize the dynamic properties of the water surface, the surface-pressure isotherm, the equilibrium (Gibbs) surface elasticity E_0 and the surface viscosity μ_s were measured *in situ* for each concentration of surfactant. (The quantity known as the surface viscosity is the sum of the surface shear and dilational viscosities.) Only a brief description of the equipment and techniques is given here; readers interested in a more detailed account are referred to Liu (2002).

A Langmuir trough forms the basic apparatus for all surface-property measurements. The trough (see figure 3) is rectangular in shape when viewed from above (50 cm by 20 cm) and is supported by a frame made of aluminum tubes. The inside surface of one end and the two long sides of the frame are lined with pieces of Teflon 1.27 cm thick that extend vertically 1 cm below the bottom of the frame. The fourth side of the trough consists of a Teflon bar 3 mm thick that spans the width of the trough. At each end of this barrier, a small spring surrounded by a small piece of thin Teflon sheet is used to make a seal against the fixed Teflon side walls of the trough. This barrier is attached to a programmable mechanism that moves the barrier horizontally in a manner that changes the area of the water surface enclosed by the trough. As explained below, the barrier is used to compress the water surface in the measurement of the surface-pressure isotherm and to create longitudinal waves in the measurements of the surface elasticity and the viscosity.

The surface tension was measured with a Whilhelmy plate tensiometer (ST9000, manufactured by NIMA Technology). In these measurements the Langmuir trough was lowered onto the water surface with the barrier positioned at far right, as seen

in figure 3, and the Whilhelmy plate was placed inside the Langmuir trough near the end farthest from the movable barrier. The initial surface-tension reading is the ambient surface tension σ_0, and the surface-pressure isotherm is the curve of $73.0-\sigma$ versus $\ln(A/A_0)$ obtained by measuring the surface tension while moving the barrier slowly to the left, as seen in figure 3 (A_0 is the initial area inside the Langmuir trough, A is the area in the trough at any time and σ is the surface tension corresponding to A).

The values of E_0 and μ_s were obtained at each ambient surfactant condition from measurements of the propagation characteristics of longitudinal surfactant waves. The apparatus and methods were similar to those described in Miyano *et al.* (1983), Ting *et al.* (1984) and Mass & Milgram (1998). There is some controversy over the accuracy of measuring E_0 and μ_s with this method; see Edwards *et al.* (1991). However, it was used in our experiments because of the similarity of the generation of longitudinal waves in this measurement technique to the two-dimensional compression of the water surface at the gravity wave crest as it travels along the wave tank.

For each surfactant condition, longitudinal waves were generated with five or more frequencies, ranging from 0.2 to 1.5 Hz, and with amplitudes of the barrier motion ranging from 0.5 mm for the highest frequencies to 5 mm for the lowest frequencies. This frequency range is well suited to the measurement of the frequency-independent parameters E_0 and μ_s using the longitudinal-wave method described herein. The longitudinal waves were measured by a capillary-wave propagation technique at five distances from the longitudinal-wave generator. From the data for each frequency, the exponential damping coefficient and the wave number were extracted. This data was used to calculate the Gibbs or equilibrium elasticity E_0, the surface excess viscosity μ_s and the surface-to-bulk-diffusion time constant, by fitting the theoretical dispersion relationship of the longitudinal waves as derived by Hansen & Ahmad (1971) to the data. It was found that the surface-to-bulk-diffusion time constant was of the order of minutes for all conditions and therefore that the surfactant can be considered as insoluble during the wave-breaking time scale, which is 1 s. This conclusion was verified in one of the SDS cases by compressing the surface to a constant value and measuring the surface tension as the SDS surface concentration returned to ambient by desorption to the bulk fluid. By fitting an exponential decay law to the data, a desorption time constant equal to 8 minutes was found.

2.5. *Description of data sets*

In this paper, results are presented for wave-breaking experiments in 'clean' water and in solutions having four different bulk concentrations of Triton X-100 and four different bulk concentrations of SDS. At each concentration of Triton X-100 or SDS, the surface dynamic properties and the crest-profile histories for each of the five breaking conditions mentioned in § 2.1 were measured. Each breaking-wave measurement was repeated three or more times. All the Triton X-100 solutions were made using a single tank of water over a period of five days. Rhodamine B, a fluorescent dye, was mixed with the water at a concentration of 3 p.p.m. for visualization purposes. On the first day of the measurements, with zero bulk concentration of Triton X-100 (clean-water), the ambient surface tension, the surface-pressure isotherms and the crest-profile histories of the breakers were measured (the data from the first measurement is denoted CLEAN). After these measurements, Triton X-100 was added to the water. On the following day, a set of measurements of the ambient surface tension, the surface-pressure isotherms, the equilibrium elasticity, the surface viscosity and the crest-profile histories of the breakers was taken (data

	TX1	TX2	TX3	TX4	SDS1	SDS2	SDS3	SDS4
$C \times 10^5$ (mol l^{-1})	0.21	0.75	1.28	3.41	1.6	6.0	19.4	41.7
σ_0 (mN m^{-1})	61.4	46.1	40.6	32.7	62.1	52.1	45.9	40.1
E_0 (mN m^{-1})	–	48.97	49.07	49.08	43.68	31.7	25.21	22.8
μ_s (mN s m^{-1})	–	1.45	1.30	1.02	2.05	1.03	0.61	0.57

TABLE 2. The surface dynamic properties at different Triton X-100 or SDS concentrations. The bulk concentration, the ambient surface tension, the equilibrium elasticity and the surface excess viscosity are represented by C, σ_0, E_0 and μ_s respectively. Values of E_0 and μ_s were not measured at the lowest concentration (TX1) owing to experimental difficulties.

set TX1). This procedure (adding Triton X-100 at the end of the day and taking measurements on the following day) was repeated three more times to obtain three additional data sets, TX2, TX3 and TX4, corresponding respectively to the three increasing Triton X-100 concentrations.

As in the Triton X-100 experiments, all SDS solutions were made using a single tank of water. Rhodamine 6G, another fluorescent dye, was mixed with the water at a concentration of 0.1 p.p.m. for visualization purposes. On the first day, as for the clean-water measurements in the Triton X-100 experiments, data were taken with zero bulk concentration of SDS to verify the repeatability of the wave behaviour and to obtain a basis for comparison with the data to be taken in solutions of SDS. After these initial measurements, SDS was added to the tank water. Procedures identical to the experiments with Triton X-100 were followed to obtain four data sets, SDS1, SDS2, SDS3 and SDS4, corresponding respectively to the four increasing SDS concentrations.

The surfactant conditions described in Liu & Duncan (2003) were from a fifth experiment using the same tank of SDS solution. After the test with solution SDS4 and without adding additional SDS to the tank, a period of three days was allowed to pass. During this time, the surface dynamic properties in the tank changed (most likely owing to bacterial growth): while the ambient surface tension and the surface elasticity remained nearly constant, the surface viscosity increased by a factor 3 and the slope of the surface-pressure isotherm increased in the region of the highest surface compression. These changes in the surface dynamic properties caused the wave behaviour to change from the spilling breaker found in SDS4 to the plunging breaker described in Liu & Duncan (2003).

3. Surface property results

Various surface properties for Triton X-100 and SDS are given in table 2 and shown in figures 4(*a–d*) and 4(*e–h*), respectively. Plots of the equilibrium (ambient) surface tension σ_0 at the air–water interface as a function of the logarithm of the bulk concentration of Triton X-100 or SDS are given in figures 4(*a*) and 4(*e*) respectively. The negatively sloped straight lines are least-square fits to the four points in each plot. These straight lines fit the data well, indicating that the surface tension decreases logarithmically with increasing surfactant concentration. These data are qualitatively consistent with the data given by Göbel & Joppien (1997) for Triton X-100 and de la Maza & Parra (1996) for SDS in carefully controlled table-top experiments using distilled water and highly purified surfactants. The quantitative differences between

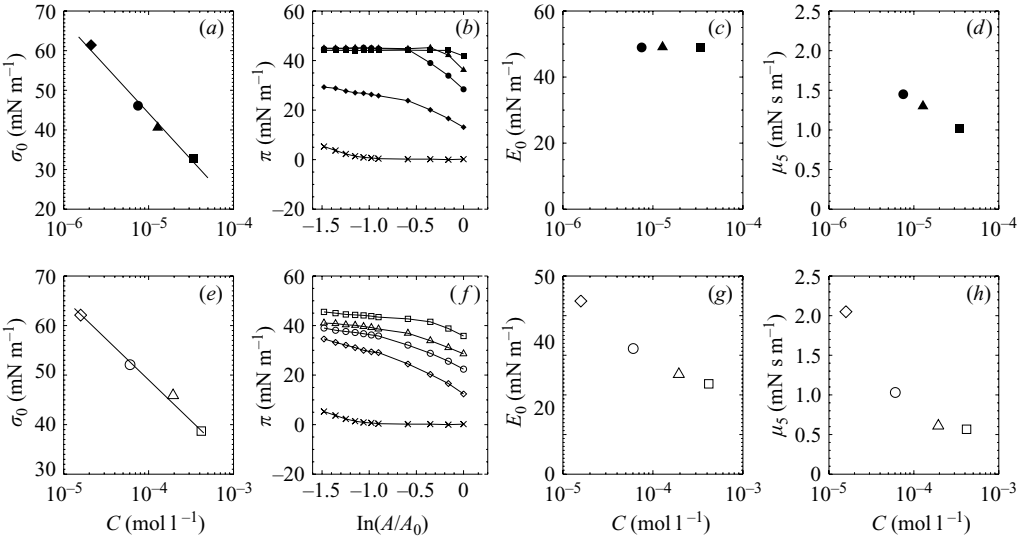

FIGURE 4. The surface dynamic properties of Triton X-100 and SDS solutions: ×, CLEAN; ◆, TX1; ●, TX2; ▲, TX3; ■, TX4; ◇, SDS1, ○, SDS2, △, SDS3; and □, SDS4. See table 2 for the surfactant concentrations. (*a*), (*e*) The equilibrium surface tension σ_0 (mN m^{-1}) vs. the surfactant bulk concentration. The straight lines are least-square fits to the four data points in each figure. (*b*), (*f*) The surface pressure $\pi = 73.0 - \sigma$ (mN m^{-1}) vs. the logarithm of the surface-area ratio A/A_0 in the Langmuir trough. A is the compressed area of the water surface in the Langmuir trough and A_0 is its initial value. (*c*), (*g*) The Gibbs elasticity E_0 (mN m^{-1}) vs. the surfactant bulk concentration. (*d*), (*h*) The surface viscosity μ_s (mN s m^{-1}) versus the surfactant bulk concentration.

the present results and the results in these papers may be caused by the factors discussed in the last paragraph of § 2.3.

The surface-pressure isotherms ($\pi = 73.0 - \sigma$ versus $\ln(A/A_0)$) for each concentration of Triton X-100 and SDS are shown in figures 4(*b*) and 4(*f*) respectively. Data for the clean-water case is also given in each figure. As can be seen from these figures, for the clean-water case the measured surface pressure has only a slight increase as the surface is compressed by a factor 4, while in the presence of Triton X-100 or SDS, even when the surface is not compressed ($\ln(A/A_0) = 0.0$), the surface pressure is above zero. For the lowest bulk concentration of Triton X-100 (TX1), the surface pressure increases monotonically as the surface area is compressed. This is true for all the SDS concentrations. For the higher bulk concentrations of Triton X-100, after the surface pressure during compression reaches a critical value, 42.5 mN m^{-1}, it remains constant as the surface is further compressed. This behaviour, which is typical of surfactants, indicates that at the onset of the region of constant surface pressure the number of surfactant molecules per unit area reaches the maximum value for a monomolecular layer (de la Maza & Parra 1996). The minimum bulk-surfactant concentration for which the entire surface-pressure isotherm is a straight horizontal line is called the critical micella concentration (CMC). As can be seen from figure 4(*b*), the concentration of Triton X-100 in TX4 is just below the CMC. This condition is not reached in any of the SDS cases, however.

The Gibbs elasticity E_0 versus the bulk concentration of the Triton X-100 and SDS solutions are shown in figures 4(*c*) and 4(*g*), respectively. As can be seen in the plots, E_0 is almost constant for the Triton X-100 cases while it decreases monotonically for the SDS solutions. The surface viscosity μ_s is plotted versus the bulk concentration of

Triton X-100 or SDS in figures 4(*d*) and 4(*h*), respectively. In both cases, μ_s decreases gradually as the surfactant bulk concentration increases.

4. Sample results of the effects of surfactants on spilling breakers with a single wave-maker motion

In this section, the data for spilling breakers generated with a single wave-maker motion (with average wave-packet frequency $f_0 = 1.15$ Hz and amplitude $A = 0.0505\lambda_0$) in water with various concentrations of surfactant are presented. Crest-profile histories and photographs of these breakers in solution TX1 are given in § 4.1. In § 4.2, the effects of the surfactants on the temporal variation of selected geometrical parameters measured from the crest profiles for clean water and, for the Triton X-100 solutions are presented. The results for breakers in the SDS solutions are qualitatively the same as those in the Triton X-100 solutions and are not shown in this section; however, the quantitative results for the SDS cases are included in the discussion in § 5.

4.1. *The crest-profile histories*

Crest-profile histories from two realizations of a breaking wave in the TX1 solution ($C = 2.1 \times 10^{-6}$ mol l^{-1} and $\sigma_0 = 61.4$ mN m^{-1}) are shown in figures 5(*a*) and 5(*b*). Lines and circles have been added to figure 5(*a*) to mark the features described below. Six photographs from the high-speed image sequence corresponding to figure 5(*a*) are given in figure 6. The surface properties of solution TX1 can be found in figure 4. As can be seen from figures 5 and 6, the breaking process still begins with the formation of a bulge on the front face of the wave. However, in the presence of Triton X-100 the bulge has flattened out and the number and amplitude of the capillary waves ahead of the toe are dramatically reduced in relation to that in clean water (compare figure 6*b* with figure 2*a* in Liu & Duncan 2003). A little while later, the toe begins to move down the wave face as it does in clean water; however, unlike the clean-water case (figure 2*b* in Liu & Duncan 2003), small-scale ripples (with wavelength $\approx$5.6 mm measured from trough to trough) form just downstream (to the right) of the toe; see the region marked by the small circle in figure 5(*a*) and image (*d*) in figure 6. After this first set of ripples is generated, the toe motion slows to near-zero speed relative to the crest. When the toe begins to move downslope again, these ripples are replaced by a train of larger ripples with wavelengths of about 9.7 mm; see the region marked by the medium-sized circle in figure 5(*a*) and images (*e*) and (*f*) in figure 6. The toe again comes to rest during the later phase of the generation of this ripple train. The ripples form a fairly uniform wavetrain that propagates with a speed a little less than that of the crest and quickly disappears by about 10 profiles after profile 6(*f*). After this point the toe again moves downslope and a third set of ripples with wavelength about 14.5 mm appears; see the largest circle in figure 5(*a*). This set of ripples varies significantly from run to run and also disappears quickly. Starting at about this time, larger ripples are generated. These ripples dominate the surface over the entire breaking region and slow down and propagate backwards over the crest in a manner similar to the clean-water case; however, in the TX1 solution the ripples are not as well defined.

A persistent feature of these breaking events in TX1 is the connected ridges marked by the three straight lines intersecting the medium-sized circle in figure 5(*a*). The negatively sloped parts of this ridge structure indicate an advancing front in the breaking zone while the middle part has a slightly positive slope, indicating that it is retreating. This retreating portion makes up one of the second set of ripples discussed

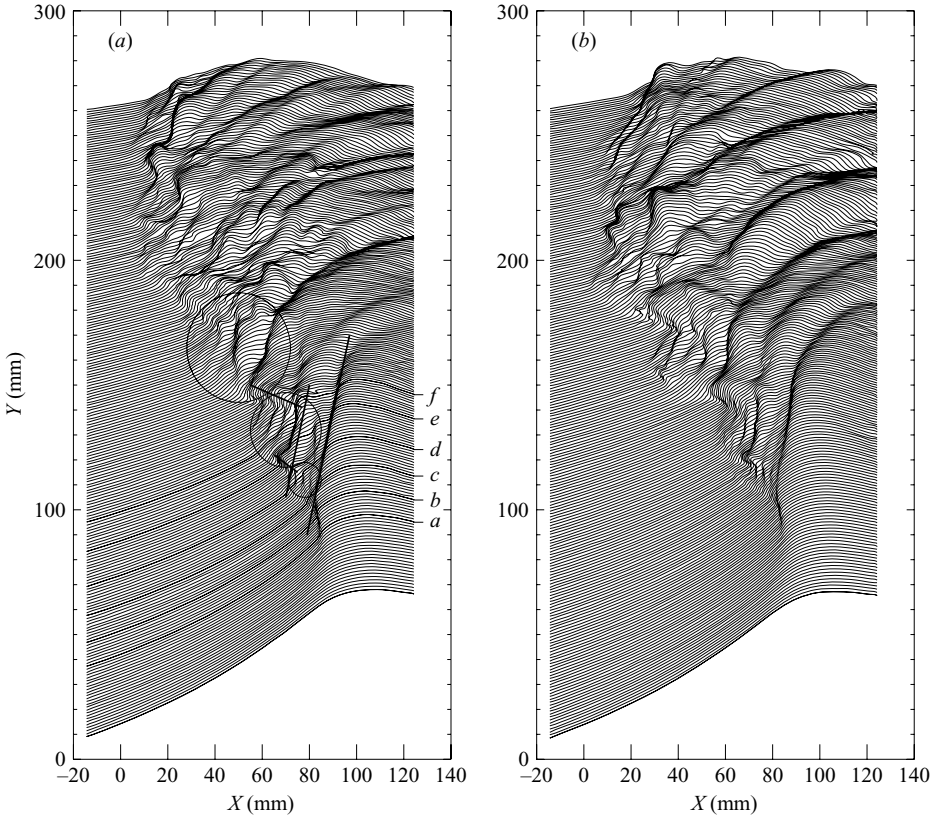

FIGURE 5. The crest-profile histories for two waves generated under identical conditions ($f_0 = 1.15$ Hz and $A = 0.0505\lambda_0$) in a Triton X-100 solution (TX1) with $C = 2.1 \times 10^{-6}$ mol l^{-1} and $\sigma_0 = 61.4$ mN m^{-1}. Each successive profile is plotted 1.0 mm above the previous profile for clarity. The profiles are shown in a reference frame fixed with respect to the wave crest. In this reference frame, the mean fluid motion is from left to right. The time between profiles is 3.33 ms. The letters at the right of (*a*) mark the crest profiles corresponding to the images in figure 6.

above. A similar ridge pattern can be seen in many profile histories from the present data set.

Another interesting feature in the profile history is the trajectory of the first trough to the left of the crest; this trough starts at the initial position of the toe. This feature is present in the clean-water case as well; however, while the trajectory has a finite radius of curvature at all points in clean-water, see figure 14 in Duncan *et al.* (1999), at this low concentration of Triton X-100 the trajectory forms a straight line with a positive slope during the time when the first two patterns of smaller-scale ripples are present; see the longest straight line in figure 5(*a*). This straight line indicates that the feature has a constant velocity that is a little slower than the crest speed. Some idea of the run-to-run repeatability of the various features of the crest-profile history can be seen by comparing figures 5(*a*) and 5(*b*). Note that the variability of the features increases with the time elapsed after the toe begins to move.

4.2. *The geometrical characteristics of the crest profiles*

In this section, the temporal histories of a number of geometrical parameters describing various features of the crest profiles for breakers generated by one

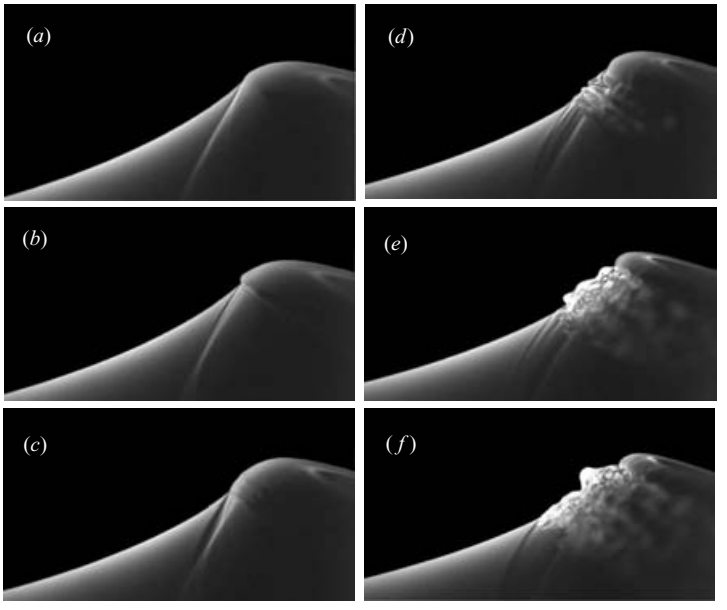

FIGURE 6. Photographs from a high-speed movie of the crest of a breaker, $f_0 = 1.15$ Hz and $A/\lambda_0 = 0.0505$ in TX1. The corresponding wave profiles are marked by (*a*)–(*f*) in figure 5. (*a*) The bulge is just beginning to form and has a flatted top surface compared with that in clean-water (figure 2*a* in Liu & Duncan 2003), $t = 0$ s; (*b*) capillary waves form upstream of the toe, but the amplitude and wavelength of the capillary waves are less than those in clean-water, $t = 0.027$ s; (*c*) the toe moves down and the capillary waves are diminished, $t = 0.056$ s; (*d*) ripples are generated between the toe and the crest, $t = 0.08$ s; (*e*) larger organized ripples are generated, $t = 0.147$ s; (*f*) the ripples propagate backwards and are left behind the crest, $t = 0.26$ s.

particular wave-maker motion ($f_0 = 1.15$ Hz, $A/\lambda_0 = 0.0505$) in 'clean' water and in all the Triton X-100 solutions are discussed. Most of the geometric parameters are defined in figure 1. They include the wavelength of the first capillary wave in front of the toe, the maximum surface height y_m and the height of the toe y_t above the mean water level, two characteristic lengths of the bulge (L_m and L_s), the maximum thickness of the bulge L_p and the angle of inclination of the free surface just upstream of the toe, θ. These parameters are similar to those used in Duncan *et al.* (1999). They are plotted against the non-dimensional distance X/λ_0, where $X = Ut$ is the distance from a reference position in the tank to the horizontal position of the crest at the instant at which each image was recorded by the camera. The reference position, $X = 0$, was chosen in each movie as the crest location in the first frame where the toe was discernible. Since clear meanings of y_m, L_s and L_m depend on the existence of a smooth crest region, the data were plotted only up to the point in time when the first ripple travels over the crest. As can be seen from the profile-history plots (figure 5), the toe is still moving downslope at this time.

As mentioned above, the capillary waves that appear upstream of the toe in the clean water case are dramatically reduced in all surfactant conditions reported herein. In fact, the amplitudes of these waves are not measurable by the techniques used in this study. The only measurable quantity describing these capillary waves is the length of the first wave upstream of the toe, i.e. the distance from the toe to the first trough of the capillary wavetrain. The length of this wave is 3.4 mm in the clean-water case.

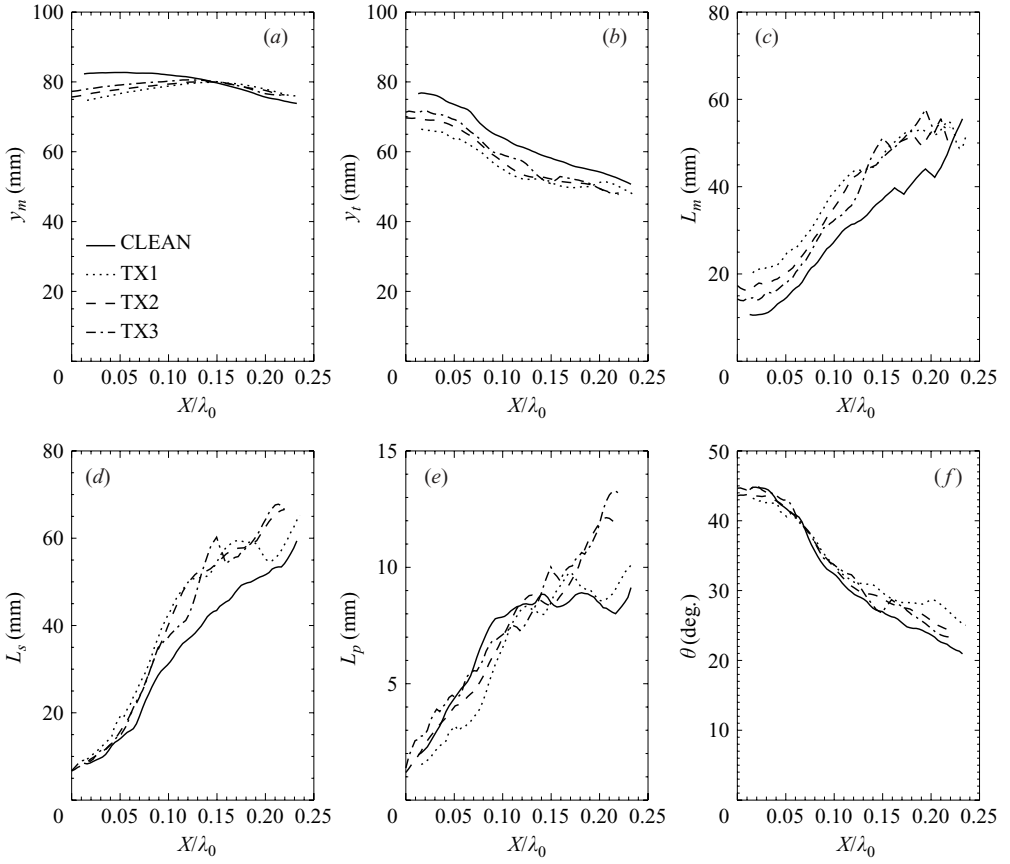

FIGURE 7. The geometrical parameters describing the spilling breakers ($f = 1.15$ Hz and $A = 0.0505\lambda_0$) in Triton X-100 solutions vs. X/λ_0; $X/\lambda_0 = 0$ is the position of the wave in the tank where the bulge and toe are just barely visible. (*a*) The crest height, y_m; (*b*) the toe height, y_t; (*c*) the bulge length from the toe to the crest, L_m; (*d*) the bulge length along the tangent, L_s; (*e*) the bulge thickness, L_p; (*f*) the angle (relative to the horizontal) of the tangent to the mean surface just upstream of the toe, θ. Estimates of the errors in the extraction of this geometrical information from the images and of the RMS error from multiple runs are given at the end of § 2.2.2.

In solution TX1, this wavelength was reduced to 2.4 mm. In the other Triton X-100 solutions the capillary wavelengths were not measurable since the capillary waves were too small in amplitude to be visible in the images.

Figure 7 shows the effects of Triton X-100 on the histories of the geometric parameters in four solutions (CLEAN, TX1, TX2 and TX3). (The breaking waves measured in solution TX4 changed gradually during the day of the experiment and therefore were not included in the comparisons in this paper.) Each line plotted in figure 7, and in all the other parameter plots, corresponds to the average data from three separate experimental runs. The ambient surface tensions varied from 73 mN m^{-1} for the CLEAN data set to 40.6 mN m^{-1} for the TX3 data set. The reference position, $X = 0$, is located $(5.35 \pm 0.02)\lambda_0$ away from the back face of the wave maker in all cases, regardless of the bulk concentration of Triton X-100.

The histories of the crest height y_m are plotted in figure 7(*a*). As can be seen from the plot, in all cases the crest height varies smoothly even through the point when

the toe starts to move down the front wave face at $X/\lambda_0 \approx 0.05$; see below. The maximum crest height for the clean-water case is 82 mm and occurs at $X = 0.06\lambda_0$. All three data sets with Triton X-100 have the nearly the same maximum value, 80 mm, at $X = 0.14\lambda_0$. Interestingly, in all four cases the X-location of the maximum crest height is past the point where the toe begins to move. Also, it should be noted that the rate of increase of y_m with X before the point of maximum crest height decreases with increasing Triton X-100 concentration.

The histories of the toe height y_t, given in figure 7(*b*), are quite different from those of the crest height. As can be seen from the figure, y_t varies in nearly the same manner in all cases: for $X/\lambda_0 < 0.05$, y_t decreases slowly; for $0.05 < X/\lambda_0 < 0.12$, the rate of decrease increases and quickly reaches a constant value; for $X/\lambda_0 > 0.12$, y_t decreases more slowly and with greater variation along each curve. The point $X = 0.05\lambda_0$ marks the beginning of the toe motion seen in the profile histories. The initial toe height in clean water is 76 mm while the initial toe heights in the presence of Triton X-100 are all less than the clean-water value. Interestingly, as the bulk concentration of Triton X-100 increases, the initial toe height increases from 66 mm for TX1 to 72 mm for TX3. The large variations in y_t along each curve in the range $X/\lambda_0 > 0.12$ indicate a larger random component of the toe motion in this phase of the breaking process.

Figures 7(*c*) and 7(*d*) show the histories of the bulge lengths L_m and L_s, respectively. The length L_m is the distance from the toe to the highest point on the wave profile, while the length L_s is the distance from the toe to the surface profile along the crest following the tangent to the smoothed water surface upstream of the toe. This smoothing was accomplished by fitting a fourth-order polynomial to the profile data in this region in order to eliminate the capillary waves, see figure 1. As in the plots of y_t, the curves can be divided into three regions: $X/\lambda_0 < 0.05$, $0.05 < X/\lambda_0 < 0.12$ and $X/\lambda_0 > 0.12$. Both L_m and L_s increase relatively slowly from $X/\lambda_0 = 0$ up to about $X/\lambda_0 = 0.05$, where the toe motion starts. After this point, they increase more rapidly until the point $X/\lambda_0 = 0.12$ where, judging by the appearance of the free surface in the movies, the flow becomes turbulent. Both L_m and L_s increase more slowly after this point. Note that, for $X/\lambda_0 > 0.12$, ripples generated between the toe and the crest begin to travel downstream over the crest, thus creating fluctuations in the L_m and L_s data that are large compared with the fluctuations for $X/\lambda_0 < 0.12$. The L_m-curves have essentially zero slope at $X = 0$ and their slope increases slowly up to $X = 0.05\lambda_0$. The initial value of L_m is 10 mm in the clean-water case and is 20 mm at the lowest concentration of Triton X-100 (TX1). It decreases as the bulk concentration of Triton X-100 increases. In contrast, the initial value of L_s is about 7 mm in all cases and from $X = 0$ to $X = 0.05\lambda_0$ all four curves fall on the same nearly straight line. For $0.5 < X/\lambda_0 < 0.12$ the slopes of all three L_s-curves in Triton X-100 are nearly the same and are greater than that for the clean-water case.

Figure 7(*e*) shows the histories of the bulge thickness L_p, which is the maximum distance from the line L_s to the water surface on the bulge, measured in the direction normal to L_s. As can be seen from the plot, the initial bulge thicknesses range from 1 mm to 2 mm. From these initial values, the bulge thicknesses increase in a nearly linear fashion until $X/\lambda_0 = 0.12$ for each concentration. The slope of this linear line is highest for the clean-water case. After $X/\lambda_0 = 0.12$, the bulge thicknesses attain a constant value of about 8.5 mm for the CLEAN and TX1 cases but continue to increase at nearly the same rate for the TX2 and TX3 cases. The larger fluctuations in the data for $X/\lambda_0 > 0.12$ occur because ripples are moving over the wave crest.

The histories of the angle (θ, measured relative to the horizontal) of the tangent to the smoothed water surface ahead of the toe are plotted in figure 7(*f*). As can

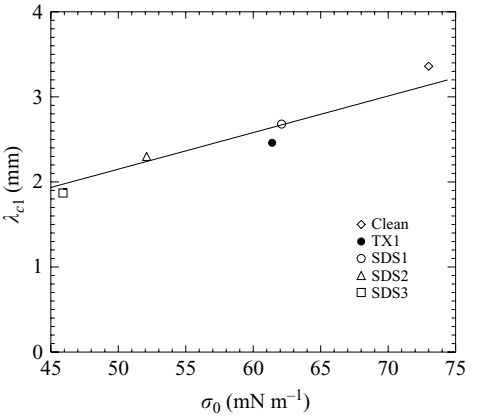

FIGURE 8. Length of the first capillary wave, λ_{c1}, versus the ambient surface tension σ_0.

be seen in the figure, the curves for θ are nearly the same in all four cases and are similar to those reported in Duncan *et al.* (1999). During the time before the toe starts to move down the wave face, this angle is nearly constant at about 43°. Once the toe begins to move, the angles decrease rapidly. The angles are much higher than the corresponding steepest angle found on the face of a limiting-form Stokes wave, i.e $\theta = 30°$; the waves in this study are highly asymmetric with the front face much steeper than the rear face.

5. Discussion

As reported in § 4, the wave-crest profiles of the breakers generated by one particular wave-maker motion vary from one surfactant condition to another. The difficulty in exploring the physics of surfactant effects on the breaking process is that changes in surfactant concentration and species typically alter all the surface dynamic properties at the same time. However, from the present data set it is possible to shed at least some light on the relative importance of these parameters. In this section, the length of the first capillary wave upstream of the toe is discussed first, in § 5.1. This is followed in § 5.2 by a discussion of the shape of the bulge and in § 5.3 by a discussion of the scaling of the breaker geometric parameters discussed previously with various length scales based on the surface dynamic properties.

5.1. *The first capillary wave*

As pointed out above, in the presence of surfactants the capillary waves found upstream of the toe have a shorter wavelength and a much smaller amplitude than those found in the clean-water case. A plot of the length of the first wave upstream of the toe (at the moment just before the toe starts to move) versus the ambient surface tension is shown in figure 8 for all conditions where this wavelength is measurable, for $A/\lambda_0 = 0.0505$ and $f_0 = 1.15$ Hz. As can be seen from the figure, the data follows a nearly linear relationship and a least-squares fit of the equation $\lambda = m\sigma_0$ to the data yields the line with $m = 0.043\,\mathrm{m^2\,N^{-1}}$ plotted in the figure. It is well known that the phase speed c of capillary waves in the presence of surfactants depends primarily on the surface tension. In still water, the dispersion relationship from linear theory is

$$c^2 = \frac{\sigma_0}{\rho}\frac{2\pi}{\lambda},$$

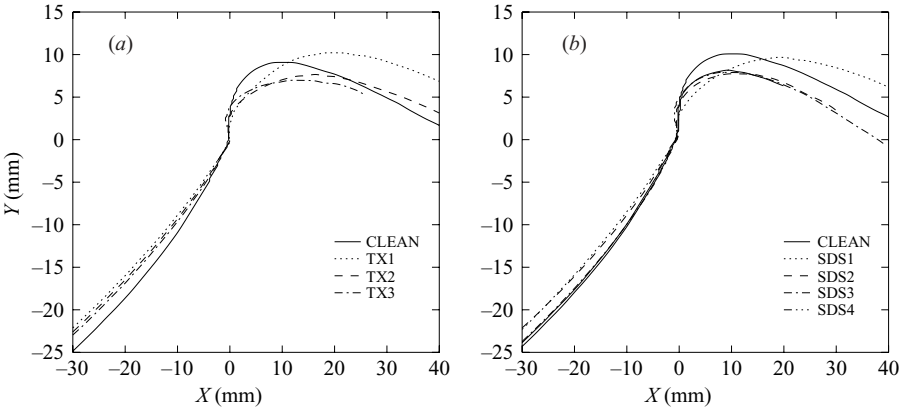

FIGURE 9. Profiles of the breakers at times just before the toe begins to move down the wave crest ($f_0 = 1.15$ Hz and $A = 0.0505\lambda_0$). (a) Clean-water and the solutions TX1, TX2 and TX3. (b) Clean-water and all the SDS solutions. In order to facilitate comparisons of the crest shapes, the profiles in each figure have been aligned at the toe.

where c is the capillary-wave phase speed. Since the capillary waves on the breakers are stationary relative to the crest, the phase speed of the waves relative to still water, c, must equal the magnitude q of the underlying fluid velocity. Thus, the linear relationship between surface tension and wavelength found in the data indicates that

$$\frac{2\pi}{\rho q^2} = 0.043$$

or $q = 38.2\,\mathrm{cm\,s^{-1}}$. In other words these waves, which are stationary when viewed in the reference frame fixed with respect to the crest, reside in an area with nearly the same flow speed for all conditions discussed herein.

The reduction in the amplitude of the capillary waves may be attributed to either a higher damping rate or a reduced generation mechanism. The effect of surfactants on the damping of small-amplitude capillary waves in otherwise calm water has been explored theoretically and experimentally by a number of authors. In clean water, the amplitude of capillary waves decreases exponentially with the coefficient $2\nu k^2$, where ν is the kinematic viscosity of water and k is the wavenumber, $2\pi/\lambda$. In the presence of surfactants this damping rate is increased, primarily owing to the effects of the surface elasticity. Calculations using equations (13) from Cini & Lombardini (1978) with the measured wavelengths in figure 8 and the measured values of E_0 in table 2 (for cases SDS1, SDS2 and SDS3) indicate that the clean-water damping exponent increases by a factor of about 2 in the present surfactant cases. Thus, it is feasible that the diminished amplitudes compared with the clean- water case are due to the increased damping caused by surface elasticity. Theoretical exploration of the reduced potential for generation of capillary waves is not a simple matter since, to date, estimates of these amplitudes have been made only through large-scale numerical calculation.

5.2. *The shape of the bulge*

In order to illustrate that the size and shape of the bulge vary significantly from one surfactant condition to another, two plots of the crest profiles at the instant before the toe begins to move down the wave face for a single wave-maker motion ($f_0 = 1.15$ Hz and $A/\lambda_0 = 0.0505$) are shown in figure 9. The plot on the left contains profiles for

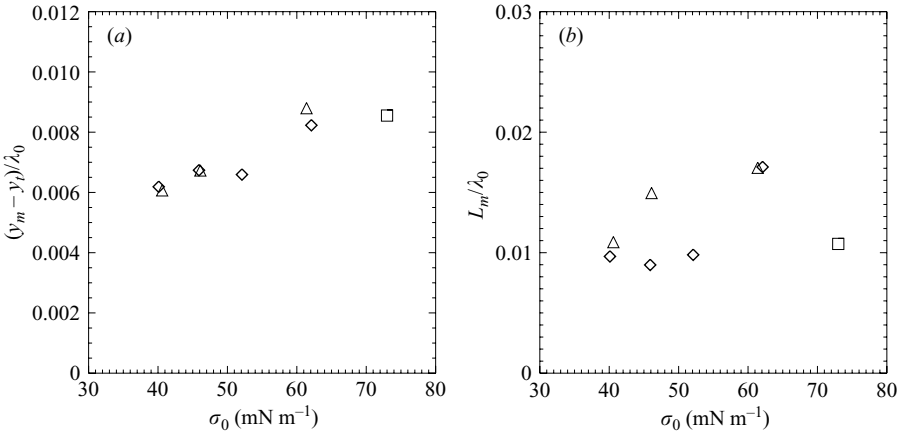

FIGURE 10. The effect of surface tension on the bulge shape for the wave-maker motion with $f_0 = 1.15$ Hz and $A = 0.0505\lambda_0$ for the solutions CLEAN, SDS1, SDS2, SDS3, SDS4, TX1, TX2 and TX3. (a) Crest-to-toe height $y_m - y_t$ and (b) crest-to-toe length L_m. ◇, SDS solutions; △, TX solutions; □, CLEAN.

clean-water and the Triton X-100 solutions and the plot on the right contains profiles for clean-water and the SDS solutions. As can be seen in the figure, the sequence of shapes of the bulge as the concentration of surfactant increases is qualitatively the same for both surfactants. In the clean-water case the bulge shape is close to a circular arc. For the lowest concentration of each surfactant (SDS1 and TX1), the bulge shape flattens out and becomes elongated in the direction along the slope of the front face of the wave. At higher concentrations of surfactants, the bulge shape returns approximately to a circular arc but with a smaller size than in the clean-water case.

In an effort to explore the physical mechanisms that control the variations in bulge shape, plots of $y_m - y_t$ and of L_m versus σ_0 at the point in time just before the toe begins to move down the wave profile are given in figures 10(*a*) and 10(*b*), respectively. As can be seen in the plots, the data for $y_m - y_t$ collapse to a single curve while the data for L_m form a separate curve for each surfactant. The collapse of the $y_m - y_t$ data may be explained partly by the leaky-capillary-jump theory proposed by Longuet-Higgins (1996). The theory is for a steady wave in a pure liquid (no surfactant) and postulates that the toe position is located at the place on the wave profile where the flow velocity in the reference frame of the crest is equal and opposite to the minimum phase speed of gravity capillary waves in still water, i.e.

$$q = 1.414(g'\gamma)^{1/4}, \tag{5.1}$$

where q is the local flow speed, $\gamma = \sigma_0/\rho$ and $g' = g\cos\alpha - \kappa q^2$ is the apparent local gravity, α and κ being the local surface slope and curvature, respectively. If q and g' are evaluated from the flow field of a Stokes wave, Longuet-Higgins (1996), numerical calculation shows that, for a given wave steepness, (5.1) would form a single curve in each of the plots in figure 10. In fact, a single curve would be formed in each of the plots if the wave steepness or even the wave shape were a function of σ_0. Thus, the fact that the $y_m - y_t$ data in figure 10(*a*) form a single curve indicates that this parameter is dominated by surface tension, in qualitative agreement with the theory. Since q was not measured in the experiments a quantitative comparison with the theory is not possible. In contrast with this result, the scatter in the data in figure 10(*b*)

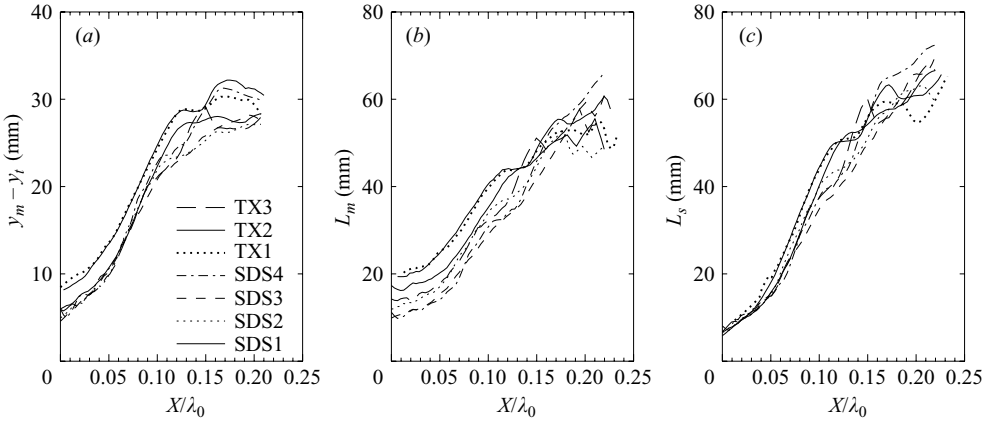

FIGURE 11. The evolution of the geometrical parameters $y_m - y_t$, L_m and L_s for breakers from a wave-maker motion with $f_0 = 1.15$ Hz and $A = 0.0505\lambda_0$ in the solutions SDS1, SDS2, SDS3, SDS4, TX1, TX2 and TX3. Estimates of the errors in the extraction of this geometrical information from the images and on the root-mean-square error from multiple runs are given at the end of § 2.2.2.

indicates that L_m must be strongly influenced by surface properties other than or in addition to the surface tension.

The reader might also have noticed from figure 9 that in solutions TX1 and SDS1 the shapes of the bulges are similar and from figure 10 that the two values of $y_m - y_t$ and the two values of L_m are nearly the same. Unfortunately, the values of E_0 and μ_s were not measured for the TX1 solution so a detailed comparison of the two cases is not possible. However, by extrapolating the curves of E_0 and μ_s in figures 4(*c*) and 4(*d*) to obtain values at the TX1 concentration, one finds that the values of E_0 and μ_s are very close to their values in SDS1.

5.3. *The scaling analysis for breakers with a single wave-maker motion*

In this subsection, the scaling of the geometrical parameters is addressed. Figure 11 shows the histories of three geometrical parameters, $y_m - y_t$, L_m, and L_s, that describe the bulge and breaking-zone shape for breakers generated a single wave-maker motion ($f_0 = 1.15$ Hz and $A/\lambda_0 = 0.0505$) in various SDS and Triton X-100 solutions. Plots for the other four wave-maker motions are similar to these but are not shown here. As can be seen from figure 11, there is a significant variation from one surfactant condition to another, the largest variations occurring in L_m.

Assuming that the parameters discussed in this paper are sufficient to describe the behaviour of the crest profile, any geometric length scale L should be a function of σ_0, E_0, μ_s, g, λ_0 and X. Here the shape of the surface-pressure isotherm is described only by its initial slope, E_0, as determined by the dynamic measurements of longitudinal waves rather than the actual slope of the statically measured isotherm. This approximation is used to narrow down the very large number of parameters in the dimensional analysis. We have performed an extensive study of the effect of the various dimensionless numbers obtained from the above-mentioned external parameters on the collapse of the data, including the three plots of figure 11. By far the most effective scaling for the curves of $y_m - y_t$, L_m and L_s is shown in figure 12, where $y_m - y_t$ and L_s are scaled by $(\sigma_0/\rho g)^{1/2}$, L_m is scaled by $(\mu_s/\rho\sqrt{g})^{2/5}$ and the abscissa of all three plots is X/λ_0. The seven curves of dimensionless $y_m - y_t$ and the six curves of dimensionless L_m show a dramatic collapse for $0 < X/\lambda_0 < 0.10$, while the

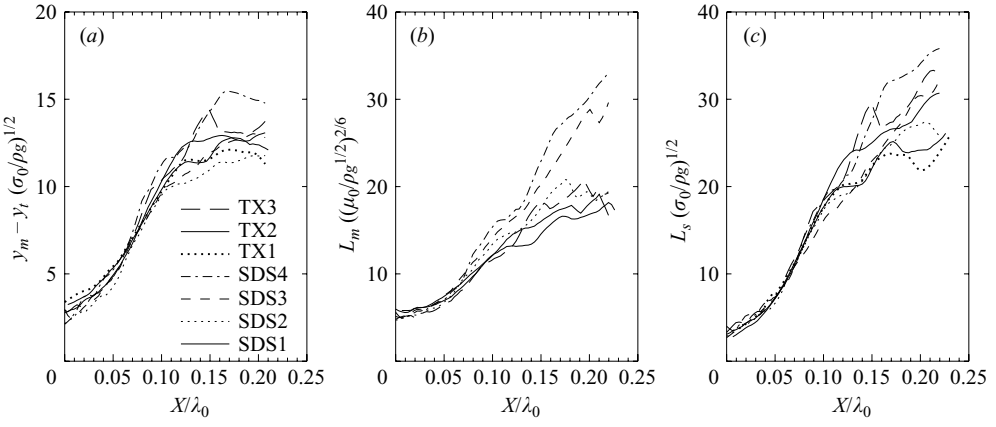

FIGURE 12. The evolution of the scaled geometrical parameters for breakers from a wave-maker motion with $f_0 = 1.15$ Hz and $A = 0.0505\lambda_0$ in the solutions SDS1, SDS2, SDS3, SDS4, TX1, TX2 and TX3. (*a*) $y_m - y_t$ is scaled by $\sqrt{\sigma_0/\rho g}$, (*b*) L_m is scaled by $(\mu_s/\rho\sqrt{g})^{2/5}$ and (*c*) L_s is scaled by $\sqrt{\sigma_0/\rho g}$.

seven curves of dimensionless L_s, which were already quite similar for $X/\lambda_0 < 0.04$, have an extended region of collapse in the dimensionless form. Apparently the success obtained with X scaled by the nominal-gravity wavelength λ_0 and with the surface-properties-based scaling of the bulge and breaking-region geometry indicates that the temporal ($X = Ut$) evolution of the geometrical parameters is dominated by the focusing of the wave packet, i.e. the average wave period. The length scale $(\sigma_0/\rho g)^{1/2}$ is proportional to the wavelength of the gravity capillary wave with minimum phase speed in a medium with surface tension σ_0, while the length scale $(\mu_s/\rho\sqrt{g})^{2/5}$ is related to the decay rate of the longitudinal waves. It is also interesting to note that while the above scalings improve the data collapse for small X/λ_0, they tend to increase the scatter in the data for $X/\lambda_0 > 0.10$. This is likely to be an indication that, as the breaking crest becomes turbulent, the surface dynamic properties become less important than inertia in determining the shape of the crest.

6. Conclusions

In the present experiments, waves similar to those studied in clean water by Duncan *et al.* (1999) were generated in the presence of ambient surfactants. Both the crest-profile histories and the ambient surface dynamic properties were measured for each surfactant condition. In the presence of surfactants at low concentrations, the breaking process described in Duncan *et al.* (1999) changes both qualitatively and quantitatively. The breaking process still starts with a bulge on the forward face, but the bulge is flatter and longer than in the clean-water case. Capillary waves still occur upstream of the leading edge (toe) of the bulge, but their amplitude and number are dramatically reduced. As the concentration of surfactant is increased but kept below the critical micella concentration (CMC), the size of the bulge diminishes and the capillary waves disappear. In all cases shown here, the start of the breaking process is initiated when the toe begins to move down the forward face of the wave. The ripple patterns generated between the toe and the crest of the wave during this phase of the breaking process vary with the concentration of surfactant.

Values for several geometrical parameters describing the crest shape of the breaking wave were obtained. These parameters have significant changes from one surfactant condition to another and the measured values of the surface dynamic properties were used in an effort to explain, at least partially, the physical processes that create these changes. It was found that the wavelength of the first capillary wave upstream of the toe decreased linearly as the ambient surface tension decreased and that the damping of the capillary waves is likely to be due to the surface elasticity. The scaling analysis of several geometrical parameters describing the bulge (L_m, L_s and $y_m - y_t$) shows that before the ripples between the toe and the crest begin to disturb the measurements, both $y_m - y_t$ and L_s apparently depend on the ambient surface tension, $(\sigma_0/\rho g)^{1/2}$ being a good length scale for these features, while L_m apparently depends on the surface viscosity, $(\mu_s/\rho\sqrt{g})^{2/5}$ being a good length scale in this case. However, none of the measured geometrical parameters scales well with length scales based on the Gibbs elasticity E_0.

The authors gratefully acknowledge the support of the the National Science Foundation, Division of Ocean Sciences, under grant number OCE0221335. We are also indebted to G. M. Korenowski for numerous conversations concerning the chemistry and dynamics of surfactants.

REFERENCES

Barger, W. R., Garrett, E. L., Mollo-Christensen, E. L. & Ruggles, K. W. 1970 Effects of an artificial sea slick upon the atmosphere and the ocean. *J. Appl. Met.* **9**, 396–400.

Bock, E. J., Hara, T., Frew, N. M. & McGillis, W. R. 1999 Relationship between air–sea gas transfer and short wind waves. *J. Geophys. Res.* **104** (C11), 821–825.

Ceniceros, H. D. 2003 The effects of surfactants on the formation and evolution of capillary waves. *Phys. Fluids* **15**, 245–256.

Ceniceros, H. D. & Hou, T. Y. 1999 Dynamic generation of capillary waves. *Phys. Fluids* **11** (5), 1032–1050.

Cini, R. & Lombardini, P. P. 1978 Damping effect of monolayers on surface wave motion in a liquid. *J. Colloid Interface Sci.* **652**, 387–389.

Coakley, D. B. 1997 Surface shape of laboratory-generated steady breaking waves. PhD thesis, University of Maryland, College Park.

Cox, C. X. & Munk, W. H. 1954 Statistics of the sea surface derived from sun glitter. *J. Mar. Res.* **13**, 198–227.

Creamer, D. C. & Wright, J. A. 1992 Surface films and wind wave growth. *J. Geophys. Res.* **97**, 5221–5229.

Dabiri, D. & Gharib, M. 1997 Experimental investigation of the vorticity generation within a spilling water wave. *J. Fluid Mech.* **330**, 113–139.

Duncan, J. H. 2001 Spilling breakers. *Annu. Rev. Fluid Mech.* **33**, 519–547.

Duncan, J. H., Philomin, V., Qiao, H. & Kimmel, J. 1994*b* The formation of a spilling breaker. *Phys. Fluids*, **6**, S2.

Duncan, J. H., Qiao, H., Behres, H. & Kimmel, J. 1994*a* The formation of a spilling breaker. *Phys. Fluids* **6** (8), 2558–2560.

Duncan, J. H., Qiao, H., Philomin, V. & Wenz, A. 1999 Gentle spilling breakers: crest profile evolution. *J. Fluid Mech.* **379**, 191–222.

Ebuchi, N., Wawamura, H. & Toba, A. 1987 Fine structure of laboratory wind-wave surfaces studies using an optical method. *Boundary-Layer Met.* **39**, 133–151.

Edwards, D. A., Brenner, H. & Wasan, D. T. 1991 *Interfacial Transport Processes and Rheology*. Butterworth-Heinemann.

Ermakov, S. A., Zujkova, A. M., Panchenko, A. R., Salshin, S. G., Talipova, T. G. & Titov, V. I. 1986 Surface film effect on short wind waves. *Dyn. Atmos. Oceans* **10**, 31–50.

Frew, N. M. 1997 The role of organic films in air–sea gas exchange. In *The Sea Surface and Global Change* (ed. P. S. Liss & R. A. Duce), pp. 121–172. Cambridge University Press.

Göbel, J. G. & Joppien, G. R. 1997 Dynamic interfacial tensions of aqueous triton X-100 solutions in contact with air, cyclohexane, n-heptane, and n-hexadecane. *J. Colloid Interface Sci.* **191**, 30–37.

Hansen, R. S. & Ahmad, J. 1971 Waves at interfaces. *Progr. Surface Membrane Sci.* **4**, 1–56.

Hühnerfuss, H., Alpers, W., Garrett, W. D., Lange, P. A. & Stolte, S. 1983 Attenuation of capillary and gravity waves at the sea by monomolecular organic surface films. *J. Geophys. Res.* **88**, 9809–9816.

Lin, J. C. & Rockwell, D. 1994 Instantaneous structure of breaking waves. *Phys. Fluids* **6**, 2877–2879.

Lin, J. C. & Rockwell, D. 1995 Evolution of quasi-steady breaking waves. *J. Fluid Mech.* **302**, 29–44.

Liu, X. 2002 An experimental investigation of the effects of surfactants on spilling breakers. PhD thesis, University of Maryland, College Park.

Liu, X. & Duncan, J. H. 2003 The effects of surfactants on spilling breaking waves. *Nature* **421**, 520–523.

Lombardini, P. P., Fiscella, B., Trivero, P. & Garrett, W. D. 1989 Modulation of the spectra of short gravity waves by sea surface films: slick detection and characterization with a microwave probe. *J. Atmos. Ocean. Technol.* **6**, 882–889.

Longuet-Higgins, M. S. 1974 Breaking waves in deep or shallow water. In *tenth Symposium on Naval Hydrodynamics*. Office of Naval Research, ACR-204, 597–605.

Longuet-Higgins, M. S. 1992 Capillary rollers and bores. *J. Fluid Mech.* **240**, 659–679.

Longuet-Higgins, M. S. 1994 Shear instability in spilling breakers. *Proc. R. Soc. Lond.* A **446**, 399–409.

Longuet-Higgins, M. S. 1996 Capillary jumps on deep water. *J. Phys. Oceanogr.* **96**, 1957–1965.

Longuet-Higgins, M. S. 1997 Progress towards understanding how waves break. *21st Symp. Nav. Hydrodyn. Trondheim, Norway, June 1996*, pp. 7–28.

Longuet-Higgins, M. S. & Dommermuth, D. G. 1997 Crest instabilities of gravity waves. Part 3. Nonlinear development and breaking. *J. Fluid Mech.* **336**, 33–50.

Lucassen, J. 1981 Effect of surface-active material on the damping of gravity waves: a reappraisal. *J. Colloid Interface Sci.* **85** (2), 52–58.

Mass, J. T. & Milgram, J. H. 1998 Dynamic behaviour of natural sea surfactant films. *J. Geophys. Res.* **103** (C), 15 695–15 715.

de la Maza, A. & Parra, J. L. 1996 Alterations in phospholipid bilayers caused by sodium dodecyl sulphate/Triton X-100 mixed systems. *Colloid Polymer Sc.* **274**, 253–260.

Mitsuyasu, H. & Honda, T. 1984 The effects of surfactant on certain air–sea interaction phenomena. In *Wave Dynamics and Radio Probing of the Ocean Surface* (ed. O. M. Phillips & K. Hasselmann), pp. 95–115. Plenum.

Miyano, K., Abraham, B. M., Ting, L. & Wasan, D. T. 1983 Longitudinal surface waves for the study of dynamic properties of surfactant systems, I. Instrumentation. *J. Colloid Interface Sci.* **92**(2), 297–302.

Okuda, K. 1982 Internal flow structure of short wind waves, Part I. On the internal vorticity structure. *J. Oceanogr. Soc. Japan* **38**, 28–42.

Qiao, H. & Duncan, J. H. 2001 Gentle spilling breakers: flow field at the crest. *J. Fluid Mech.* **439**, 57–85.

Rapp, R. & Melville, W. K. 1990 Laboratory measurements of deep water breaking waves. *Phil. Trans. R. Soc. Lond.* A **331**, 735–800.

Tang, S. & Wu, J. 1992 Suppression of wind-generated ripples by natural films: a laboratory study. *J. Geophys. Res.* **97** (C4), 5301–5306.

Ting, L., Wasan, D. T., Miyano, K. & Xu, S. Q. 1984 Longitudinal surface waves for the study of dynamic properties of surfactant systems, II. Air–solution interface. *J. Colloid Interface Sc.* **102** (2), 248–259.

Tulin, M. P. 1996 Breaking of ocean waves and downshifting. In *Waves and Nonlinear Processes in Hydrodynamics* (ed. J. Grue *et al.*), pp. 177–190. Kluwer.

Tulin, M. P. & Waseda, T. 1998 Laboratory observations of wave group evolution, including breaking effects. *J. Fluid Mech.* **378**, 197–232.

Uz, B. M., Donelan, M. A., Hara, T. & Bock, E. J. 2002 Laboratory studies of wind stress over surface waves. *Boundary-Layer Met.* **102** (2), 301–331.

Yao, Y., Wang, P. & Tulin, M. P. 1996 Surface tension effects on breaking waves – LONGTANK simulation. *Tech. Rep.* 95-132. University of California, Santa Barbara.